The Astrophysical Journal Letters, 970:L23 (15pp), 2024 July 20 https://doi.org/10.3847/2041-8213/ad5f1b

X-Ray Quasi-periodic Eruptions and Tidal Disruption Events Prefer Similar Host Galaxies

T. Wevers[1], K. D. French[2], A. I. Zabludoff[3], T. C. Fischer[4], K. Rowlands[4,5], M. Guolo[6], B. Dalla Barba[7,8,9], R. Arcodia[10], M. Berton[7], F. Bian[7], I. Linial[11,12], G. Miniutti[13], and D. R. Pasham[10]
[1] Space Telescope Science Institute, 3700 San Martin Drive, Baltimore, MD 21218, USA; twevers@stsci.edu
[2] Department of Astronomy, University of Illinois, 1002 W. Green Street, Urbana, IL 61801, USA
[3] Department of Astronomy and Steward Observatory, University of Arizona, 933 N. Cherry Avenue, Tucson, AZ 85721, USA
[4] AURA for ESA, Space Telescope Science Institute, 3700 San Martin Drive, Baltimore, MD 21218, USA
[5] William H. Miller III Department of Physics and Astronomy, Johns Hopkins University, Baltimore, MD 21218, USA
[6] Bloomberg Center for Physics and Astronomy, Johns Hopkins University, 3400 N. Charles Street, Baltimore, MD 21218, USA
[7] European Southern Observatory, Alonso de Córdova 3107, Vitacura, Santiago, Chile
[8] Università degli studi dell'Insubria, Via Valleggio 11, Como 22100, Italy
[9] Osservatorio Astronomico di Brera, Istituto Nazionale di Astrofisica (INAF), Via E. Bianchi 46, Merate (LC) 23807, Italy
[10] MIT Kavli Institute for Astrophysics and Space Research, 70 Vassar Street, Cambridge, MA 02139, USA
[11] Institute for Advanced Study, 1 Einstein Drive, Princeton, NJ 08540, USA
[12] Department of Physics and Columbia Astrophysics Laboratory, Columbia University, New York, NY 10027, USA
[13] Centro de Astrobiología (CAB), CSIC-INTA, Camino Bajo del Castillo s/n, ESAC campus, 28692 Villanueva de la Cañada, Madrid, Spain
Received 2024 June 4; revised 2024 July 3; accepted 2024 July 3; published 2024 July 19

Abstract

In the past 5 yr, six X-ray quasi-periodic eruption (QPE) sources have been discovered in the nuclei of nearby galaxies. Their origin remains an open question. We present Multi Unit Spectroscopic Explorer integral field spectroscopy of five QPE host galaxies to characterize their properties. We find that 3/5 galaxies host extended emission-line regions (EELRs) up to 10 kpc in size. The EELRs are photoionized by a nonstellar continuum, but the current nuclear luminosity is insufficient to power the observed emission lines. The EELRs are decoupled from the stars both kinematically and in projected sky position, and the low velocities and velocity dispersions (<100 km s^{-1} and $\lesssim 75$ km s^{-1}, respectively) are inconsistent with being driven by active galactic nuclei (AGNs) or shocks. The origin of the EELRs is likely a previous phase of nuclear activity. QPE host galaxies share several similarities with tidal disruption event (TDE) hosts, including an overrepresentation of galaxies with strong Balmer absorption and little ongoing star formation, as well as a preference for a short-lived (the typical EELR lifetime is $\sim$15,000 yr), gas-rich phase where the nucleus has recently faded significantly. This suggests that QPEs and TDEs may share a common formation channel, disfavoring AGN accretion disk instabilities as the origin of QPEs. If QPEs are related to extreme mass ratio inspiral systems (EMRIs), e.g., stellar-mass objects on bound orbits about massive black holes, the high incidence of EELRs and recently faded nuclei could be used to localize the hosts of EMRIs discovered by low-frequency gravitational-wave observatories.

Unified Astronomy Thesaurus concepts: Accretion (14); Galaxy mergers (608); Active galactic nuclei (16); High energy astrophysics (739)

1. Introduction

X-ray quasi-periodic eruption (QPE) sources are a recent addition to the various modes of rapid variability observed in massive black holes inhabiting galactic nuclei. Their timing and spectral properties, including quasi-periodic behavior and the emergence of an additional hot thermal component during the outburst rise, are unique among the known variability of active galactic nuclei (AGNs; Miniutti et al. 2019; Giustini et al. 2020; Arcodia et al. 2021). QPEs may relate to accretion disk instabilities (Sniegowska et al. 2020; Raj & Nixon 2021; Pan et al. 2023) or to the interaction between the supermassive black hole (SMBH; or an accretion disk surrounding it) and a stellar-mass companion. The latter class of models comes in many flavors, including repeated partial tidal disruptions (King 2022), Roche lobe overflow (Krolik & Linial 2022; Metzger et al. 2022; Lu & Quataert 2023), and star–disk or BH–disk interactions (Franchini et al. 2023; Linial & Metzger 2023; Tagawa & Haiman 2023; Zhou et al. 2024).

Observationally, several QPEs occur over the course of a long-term ($\sim$years) light-curve decline, which may be related to the tidal disruptions of stars (Miniutti et al. 2023; Arcodia et al. 2024). Some QPEs also exhibit rebrightening episodes. Other clues that hint at a potential connection between QPEs and tidal disruption events (TDEs) include the discovery of QPE-like flares in TDE candidates (Chakraborty et al. 2021; Quintin et al. 2023). From a theoretical perspective, some models require a compact accretion disk to explain the QPEs, which similarly require a TDE to render the QPEs visible (Linial & Metzger 2023).

Further similarities between QPEs and TDEs can be found in their host galaxies, which have been inferred to contain black holes smaller ($\sim 10^6\,M_\odot$) than in typical AGNs (Wevers et al. 2017; Mockler et al. 2019; Wevers et al. 2019, 2022). Wevers et al. (2022) also noted that QPEs are overrepresented among post-starburst (PSB) and quiescent Balmer strong (QBS) galaxies, which are rare ($\lesssim$0.2% and 2%, respectively) in the local Universe. TDEs are likewise known to be overrepresented

among PSB and QBS galaxies (French et al. 2016; Graur et al. 2018). A recent study of integral field spectroscopy of a large sample of PSB galaxies by French et al. (2023) revealed that of the six sources that have extended emission-line regions (EELRs) of ionized gas, one was the host galaxy of a TDE (AT2019azh) and one was host to a QPE (RX J1301). Evidence for an EELR also exists in Hubble Space Telescope (HST) narrowband imaging of the host galaxy of the QPE GSN 069, including a marginally resolved, compact (<35 pc) component and a larger-scale (∼2 kpc, all throughout the HST field of view) component (Patra et al. 2024).

Based on the presence of line ratios that require a hard, nonstellar continuum in long-slit spectroscopy of the QPE nuclei, Wevers et al. (2022) suggested that a long-lived accretion flow may play an important role in the QPE phenomenon. A study of the spatially resolved properties of the QPE host galaxies can be used to trace their merger and accretion history, which can provide further clues to the importance (or lack thereof) of AGN activity on the rate of nuclear transients such as QPEs and TDEs.

In this work we present Multi Unit Spectroscopic Explorer (MUSE) integral field spectroscopy of five QPE host galaxies. We describe the observations and data analysis in Section 2. We present the main results in Section 3, including the presence of EELRs of ionized gas with peculiar kinematics that are decoupled from the stellar motions, as well as evidence for recently faded AGNs. In Section 4 we discuss these results in the context of the connection between QPEs and TDEs based on their host galaxy preferences, which show similarities in the nuclear evolution and phase as derived from the EELR properties, as well as implications for the theoretical models invoked to explain QPEs. We present the main conclusions in Section 5.

2. Observations and Analysis

We used the MUSE (Bacon et al. 2010) instrument mounted on the Very Large Telescope Unit 4 (Yepun) to observe the host galaxies of five out of six known QPE sources (Miniutti et al. 2019; Giustini et al. 2020; Arcodia et al. 2021, 2024). MUSE integral field observations cover a $1' \times 1'$ field of view with a spatial sampling (spaxel size) of $0\farcs2$. The approximately constant spectral resolution of FWHM ≈ 2.62 Å corresponds to 165 (85) km s^{-1} at 4800 Å (9300 Å) and a velocity dispersion instrumental resolution of 70 (35) km s^{-1}. An overview of the basic source properties can be found in Table A1. Details regarding the data reduction and a full observing log are provided in Appendix A and Table A2.

Galactic foreground extinction is removed prior to the data analysis in accordance with the $E(B–V)$ values reported by Schlafly & Finkbeiner (2011) as tabulated in Table A1 and assuming $R_V = 3.1$. The reported results are not sensitive to the presence of additional intrinsic host galaxy extinction, which is expected to be low.

We use pseudo-aperture spectra (with a size equal to the typical point-spread function (PSF) FWHM of the observations in Table A2) of the nuclei to study the nuclear stellar properties. We also analyze the individual spaxel data where the signal-to-noise ratio (SNR) around 5400 Å is >5, and we create pseudo-aperture spectra in various regions of the EELRs to confirm the results of our spatially resolved analysis with higher SNR.

To analyze the morphology and stellar and ionized gas kinematics and properties, we use the penalized pixel fitting routine (PPXF; Cappellari 2023); more details are given in Appendix B. All quoted line velocity dispersions are corrected for instrumental broadening.

2.1. Kinematics and Line Fluxes

We employ the MILES single stellar population (SSP) library (Vazdekis et al. 2015) to fit the stellar continuum contribution as a linear combination of SSPs and constrain the stellar kinematics (see Appendix B for more details).

Following the determination of the best-fit SSP templates, they are subtracted before analyzing the emission lines. There is no evidence of broad emission lines (BELs) in the galaxy nuclei (see also Wevers et al. 2022), nor for multiple kinematic components to the narrow lines (see Figures B2, B3, and B4 for example spectra). We therefore use a single kinematic component, parameterized by a narrow Gaussian, to determine the velocity dispersions, velocities, and fluxes of the emission lines on the scale of the native spaxel size. Note that the PSF FWHM is generally much larger (see Table A2), so at the smallest spatial scales these measurements will be correlated. We have verified that decoupling the line widths and velocities for each emission line (or doublet) does not significantly alter the results. Similarly, the stellar continuum subtraction does not significantly alter the inferred gas kinematics because the EELRs are generally isolated from the continuum emission.

Three-color composite images including the emission-line maps and a continuum band image are shown in Figure 1 to visualize the resulting flux distributions and to study the ionized gas morphology. Zoomed-in versions of the nuclear regions of these galaxies are available in Figure B1.

2.2. Star Formation Histories

Two of the host galaxies (RX J1301 and eRO-QPE1) are spectroscopically classified as PSB (Lick index $H\delta_A > 4$ Å and EW(Hα) < 3 Å) or QBS ($H\delta_A > 1.31$ Å) galaxies (Wevers et al. 2022). In addition, the MUSE data reveal that GSN 069 and eRO-QPE2 show clear signs of ongoing star formation (SF): GSN 069 has a bright circumnuclear star-forming ring, and both GSN 069 and eRO-QPE2 show several star-forming knots tracing spiral arms (Figure 1). eRO-QPE3 is in the star-forming region of the BPT and WHAN diagrams, although the current SF rate is likely low (Figure B6).

If we assume that each host galaxy experienced a recent burst of SF, we can constrain the PSB age (age since 90% of the burst stars formed) and mass of new stars that formed by applying Bagpipes (Carnall et al. 2018, 2019) to the integrated host spectra. We assume an SF history (SFH) consisting of an old delayed exponential and a young burst exponential, a method similar to French et al. (2023). We allow the masses and ages of both components to vary, as well as the duration of the young burst component, with logarithmic priors. We assume a Kroupa (2001) initial mass function and a Calzetti dust law (Calzetti et al. 2000), allowing the attenuation to vary. Following Carnall et al. (2019), we include three terms in a Gaussian process noise model.

We find that when allowing for both a young and an old burst, all galaxies prefer the inclusion of a recent burst of SF within the past 0.2–1.3 Gyr. For RX J1301 and eRO-QPE2, our modeling prefers a sizable recent burst (Table 1). This burst has been quenched for RX J1301 (hence its PSB classification),

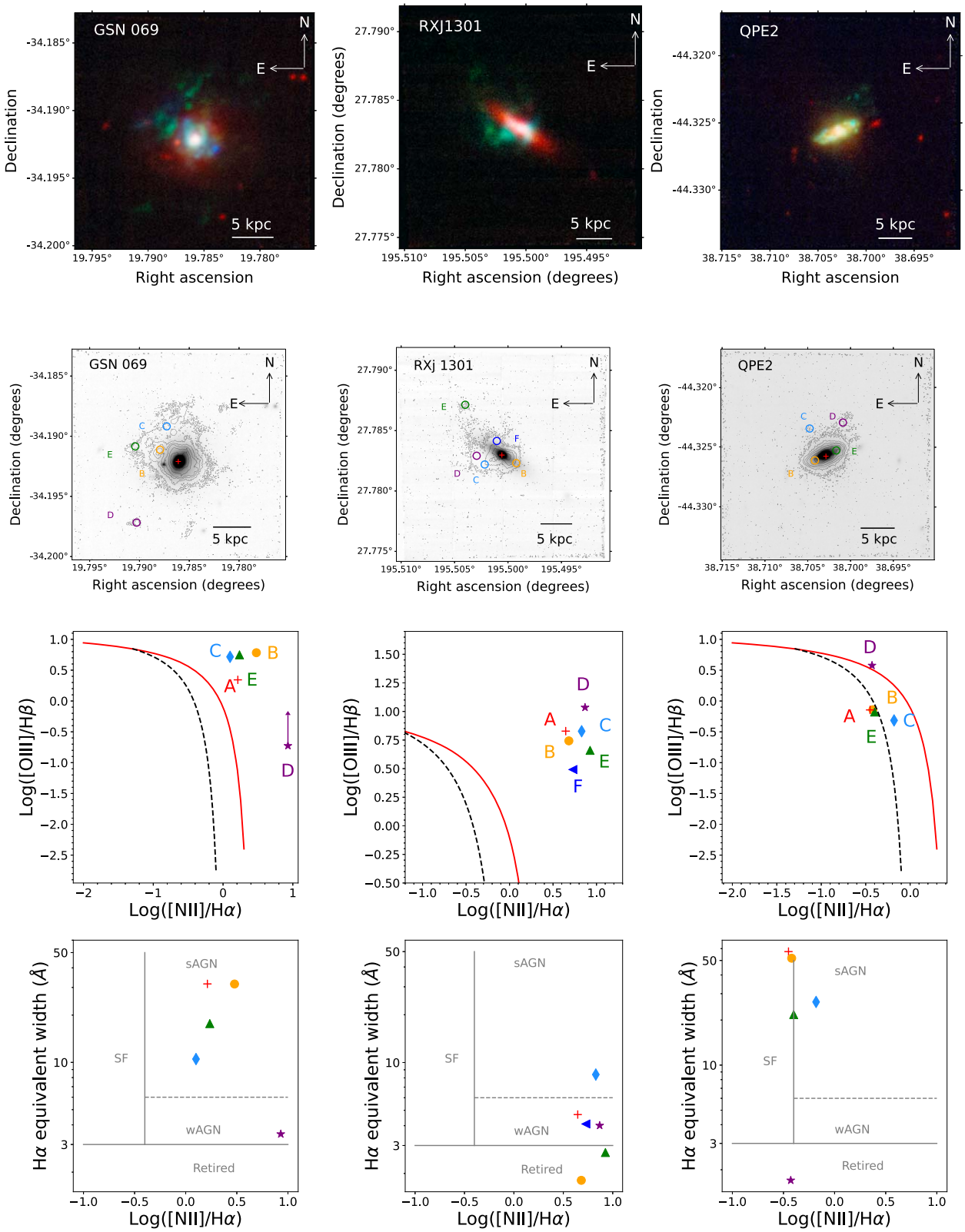

Figure 1. Images of the host galaxies. Top row: RGB color composites. The continuum is shown in red, while green hues denote Hα (QPE2) or N II (RX J1301 and GSN 069). O III is shown in blue. Zoomed-in panels can be found in Figure B1. Second row: grayscale continuum images overlaid with a contour map of the emission line. The red plus sign indicates the continuum nucleus position. Kiloparsec-scale EELRs of ionized gas are discernible in three out of five QPE hosts. This ionized gas is decoupled from the continuum emission. Third row: BPT diagram of the line ratios using the regions indicated in the panel above, after correcting for the stellar continuum component. Bottom row: WHAN diagram of the same regions.

Table 1
Overview of the QPE and EELR Properties of the Host Galaxies

Source	Class	Burst Age $\log_{10}$ (yr)	Burst Frac.	EELR	Ion. Cont. (EELR)	$R_{\rm max}$ (lt-yr)	$L_{\rm QPE,quiesc}$ (erg s^{-1})	$L_{\rm ion,min}$ (erg s^{-1})	$L_{\rm nuc,IR}$ (erg s^{-1})
GSN 069	N	Ongoing	0.045(2)	Y	Nonstellar	30,000	$3 \pm 2 \times 10^{43}$	$>6 \times 10^{42}$	$<3 \times 10^{42}$
RX J1301	PSB	8.68(1)	0.12(1)	Y	Nonstellar	9000	$2.5 \pm 0.5 \times 10^{42}$	$>2.5 \times 10^{42}$	$<1.5 \times 10^{42}$
eRO-QPE1	QBS	9.11(4)	0.066(2)	N	⋯	⋯	$5.1^{+1.6}_{-1.5} \times 10^{40}$	⋯	⋯
eRO-QPE2	N	Ongoing	0.14(2)	Y	Composite	15,000	$3^{+4}_{-2} \times 10^{43}$	$>2.5 \times 10^{42}$	4×10^{41}
eRO-QPE3	N	8.6(2)	0.014(1)	N	⋯	⋯	$<4 \times 10^{40}$	⋯	⋯

Note. Class indicates the spectroscopic classification based on the Hδ_A absorption and Hα EW: PSB, QBS, or neither (N). Burst age and fraction refer to the time since the most recent starburst and the percentage of stars formed in said starburst (see text), where numbers in parentheses denote uncertainty on the last digit. Ion. Cont. indicates the classification of the ionizing continuum, based on the BPT and WHAN diagnostic diagrams. $R_{\rm max}$ refers to the largest (projected) extent of the EELR relative to the nucleus. $L_{\rm QPE,quiesc}$ is the bolometric luminosity during QPE quiescence, taken from the literature (GSN 069, Miniutti et al. 2023; RX J1301, Giustini et al. 2024, submitted; eRO-QPE1, Chakraborty et al. 2024; eRO-QPE2, Arcodia et al. 2021; eRO-QPE3, Arcodia et al. 2024). $L_{\rm ion,min}$ is the minimum nuclear ionizing luminosity required to power the EELR; the Hα line provides the most constraining limit in all cases. $L_{\rm IR}$ is the luminosity inferred from IRAS FIR detections or upper limits.

while the burst is still ongoing for eRO-QPE2 (hence its star-forming/AGN classification; see Section 3). eRO-QPE1 had a weaker burst about a gigayear ago and has remained quenched, leading to its QBS classification.[14] The best-fit burst in eRO-QPE3 is smaller still (∼1%−2% of stars formed). Finally, the SFH of GSN 069 resembles that of eRO-QPE2, including a smaller burst fraction (5% of stars formed) where the SF has not yet been fully quenched.

3. Results

Upon inspection of the emission-line maps (Figure 1, top row), three out of five sources show EELRs that have line ratios consistent with being powered by SF or a nonstellar continuum (Figure 1, bottom two rows). We note that the sensitivity of our observations is not uniform across the sample, and the nondetections in two sources may be in part due to a sensitivity bias related to a higher redshift for eRO-QPE1 ($z = 0.0505$, the highest redshift in the sample) and/or a fainter and more compact host galaxy (eRO-QPE1 and eRO-QPE3).

3.1. Extended Emission-line Region Morphology

In Figure 1 we show continuum images of the galaxies overlaid with emission-line contours of Hα or N II (the latter is brighter in the case of GSN 069 and RX J1301). GSN 069, eRO-QPE2, and RX J1301 show EELRs on spatial scales extending up to 10 kpc from the galaxy nucleus. eRO-QPE1 and eRO-QPE3 do not show any extended ionized emission and have compact continuum morphologies (Figure A1). In the case of GSN 069 there are patchy clumps of gas bright only in N II that appear completely isolated to the south and southeast. There is no clear visual connection to the stellar light distribution. These EELRs do not appear to have a preferred directionality compared to the continuum morphology of their host galaxy, as might be expected if the gas was deposited by a previous episode of AGN activity with a galactic-scale outflow (e.g., Fischer et al. 2013) or the result of stellar feedback following a strong starburst. These morphologies are instead often (but not exclusively) seen in post-merger galaxies, where gas can be deposited at large radii as a result of splashback (Johnston et al. 2008; Schweizer et al. 2013; Weaver et al. 2018). However, there are other mechanisms that can result in extended gas distributions, including the aforementioned galactic-scale outflows, or the accretion/infall of gas from the intergalactic medium (e.g., Hafen et al. 2019).

3.2. Kinematics

Spatially resolved kinematics of the stellar and gas components are presented in Figure 2. The stellar velocity component is well behaved and displays rotation-dominated profiles in every galaxy (shown in Figure B5 in Appendix B). The central stellar velocity dispersions we measure using aperture spectra are consistent with literature values, except for RX J1301 and eRO-QPE3. For the former we find a value of 68 ± 5 km s^{-1}, compared to 90 ± 2 km s^{-1} measured using Sloan Digital Sky Survey data (Wevers et al. 2022). This is corroborated by the spatially resolved map, which has peak values around 70 km s^{-1}. For eRO-QPE3, Arcodia et al. (2024) reported a velocity dispersion of 152 km s^{-1}, while we find $\sigma_{\rm star} = 38 \pm 5$ km s^{-1}. Using the $M_{\rm BH}$–σ relation of Gültekin et al. (2009) results in a black hole mass of $M_{\rm BH} = 5.1 \pm 0.55\, M_{\odot}$ for eRO-QPE3.

The ionized gas kinematics display more disturbed patterns. In GSN 069 and eRO-QPE2, the ionized gas does appear to roughly corotate with the stellar motions globally, although there is a velocity gradient between the gas and stars in both systems. For RX J1301, the EELR appears to consist of a single kinematic component with a consistent velocity shift of +50 km s^{-1} (see Figure 2, middle panel), i.e., decoupled from the rotation of the stellar motion. This is very similar to the EELR seen in the TDE host galaxy Mrk 950 (Wevers & French 2024).

More generally, the majority of the ionized gas in these galaxies appears to have very low turbulence, with velocity dispersions that are typically <75 km $^{-1}$. We highlight that the gas in eRO-QPE2 has extremely low line widths <30 km s^{-1} throughout the galaxy and EELR. In GSN 069, there are (disconnected) regions at the edge of the EELR with velocity dispersions up to 150 km s^{-1} (compared to ∼75 km s^{-1} in the nucleus) at distances of 7–10 kpc from the center of the galaxy, although the bulk of the gas has $\sigma_{\rm gas} < 75$ km s^{-1}.

3.3. Diagnostic Diagrams

We use the emission-line ratios of these galaxies in diagnostic diagrams to understand the dominant ionization mechanism. The EELR pseudo-aperture spectra are located within the AGN region of the BPT and WHAN diagrams, shown in the bottom two rows

[14] We assume a specific SFH with a young and an old burst, but note that we do not explore other SFH scenarios that may also lead to a QBS classification without requiring a starburst.

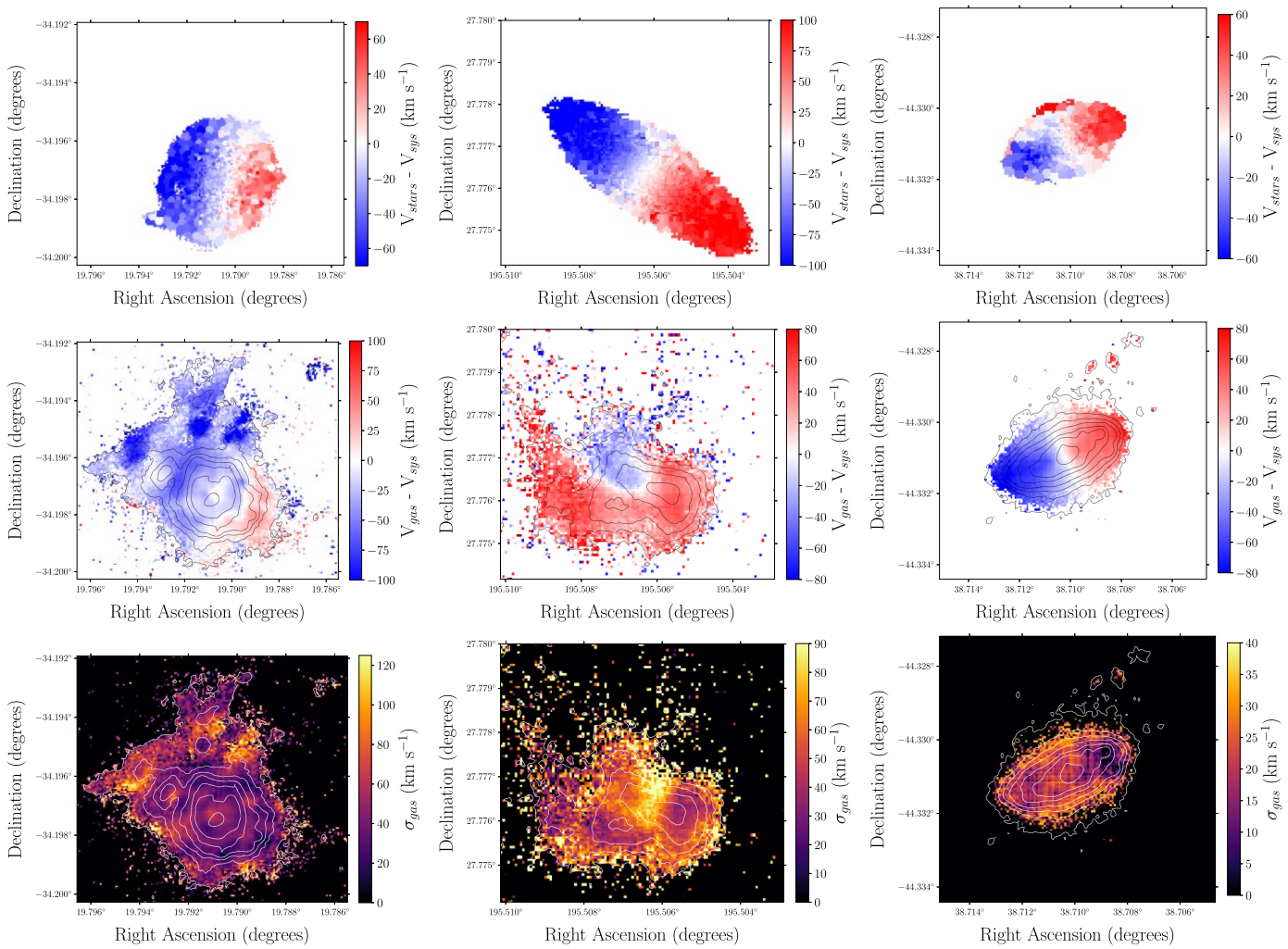

Figure 2. Spatially resolved kinematics. Shown are stellar velocity (top), gas velocity (middle), and gas velocity dispersion (bottom) maps. The contours indicate the EELR to guide the eye. The left column shows GSN 069, the middle column shows RX J1301, and the right column shows eRO-QPE2. The sky area is identical for every source across the panels to highlight the differences in EELR kinematics compared to the stellar continuum.

of Figure 1. Our results for the galactic nuclei are consistent with the conclusion by Wevers et al. (2022) that the photoionization mechanism in the QPE host galaxies is likely nonstellar in nature. For eRO-QPE3, the ionizing continuum appears to be SF dominated. We show the aperture spectra of various regions in Figures B2, B3, and B4 in Appendix B.

3.4. Constraints on the Ionizing Luminosity

The large extent of the EELRs can be used to probe the recent accretion history of the SMBHs in these galaxies. We follow Keel et al. (2017) and French et al. (2023) to estimate the required ionizing luminosity to power the observed EELR line fluxes. In the assumption of photoionization equilibrium (recombination balance), such an estimate can be made for each spaxel by taking into account the diminishing covering fraction with distance (the farther away a spaxel is from the nucleus, the higher the required ionizing luminosity for a fixed observed line flux). More quantitatively, we follow French et al. (2023) by using the Hα and Hβ emission-line luminosities $L_{\rm H}$[15] to compute two independent estimates of $L_{\rm ion,min}$ in each spaxel (see Figure B7) as follows:

$$L_{\rm ion,min} = \frac{n_{\rm rec} L_{\rm H} E_{\rm ion}}{E_{\rm H}} \frac{1}{f}. \quad (1)$$

Here f is the covering fraction in units of spaxels,

$$f = \frac{(2\ \arctan(0.5/r))^2}{4\pi}, \quad (2)$$

$n_{\rm rec}$ is the number of ionizing photons per recombination, $E_{\rm ion}$ is the ionizing energy between 13.6 and 54.6 eV (we assume that higher-energy photons will be primarily absorbed by helium), $E_{\rm H}$ is the energy per Hα or Hβ photon, and r is the distance to the nucleus.

Following Keel et al. (2012), we further use the Infrared Astronomical Satellite (IRAS) all-sky survey data (derived from the 60 and 100 μm measurements) to estimate the present-day AGN luminosity or derive upper limits. A correction for present-day SF is applied based on the distance from the SF main sequence in the BPT diagram (Wild et al. 2010). These estimates are conservative given the potential for additional extinction not probed by the Balmer decrement (see, e.g., Baron et al. 2022). The results can be found in Table 1. We

[15] Due to the relatively low SNR of spectra in individual spaxels, we do not incorporate an extinction component to estimate these line fluxes.

highlight that for every QPE host with an EELR detection we infer a present-day nuclear luminosity ($L_{\rm nuc,IR}$) that is below the luminosity required to power the most distant regions of the EELRs. In other words, if an AGN was previously present in these systems, its present-day luminosity is a factor of 2–5 lower compared to the most stringent constraints on the luminosity history provided by the EELR gas (inferred by comparing the values of $L_{\rm nuc,IR}$ and $L_{\rm ion,min}$ in Table 1). Note that the gas density, not the AGN luminosity, is likely the limiting factor for the observability of the EELR at large radii; the nuclei may have been more luminous in the past, but without more distant EELR gas we cannot constrain the luminosity history beyond the light-travel time of the EELR (in the range $(1–3)\times10^4$ yr). This is consistent with the episodic nature of AGN activity, which has typical duty cycles of $\sim10^5$ yr with rapid transitions on $\sim10^4$ yr timescales (Schawinski et al. 2015; Keel et al. 2017).

4. Discussion

Our analysis shows that four out of five QPE host galaxies have one or more peculiar properties, including the presence of a quenched starburst (a PSB phase; RX J1301), a QBS spectrum (which may indicate a weaker recent starburst; eRO-QPE1), the presence of extended ionized gas emission (Figure 2; RX J1301, GSN 069, and eRO-QPE2) that is decoupled from the stellar continuum, and/or the presence of a recently faded nuclear engine (Table 1; RX J1301, GSN 069, and eRO-QPE2). The last occurs in $\sim1/3$ of EELR-hosting galaxies (Keel et al. 2012). Except for the PSB galaxy RX J1301, no tidal tails or other visual disturbances are obvious in the stellar continuum light. Such features are typically seen in other studies of Voorwerp/faded AGNs with EELRs (e.g., Keel et al. 2015), and they can provide a robust association for a post-merger origin of the EELR gas. Further studies of larger, deeper, and higher spatial resolution samples are needed to test the tentative connection between the QPE host properties and post-merger Voorwerp/faded AGNs with EELRs.

We find a fractional incidence of EELRs in QPE host galaxies of $f_{\rm EELR}=0.6^{+0.4}_{-0.33}$ (where the uncertainties are two-sided Poisson confidence intervals; Gehrels 1986). If the nondetections in eRO-QPE1 and/or eRO-QPE3 are due to the limited sensitivity of our observations, the true value may be higher (with the caveat of small sample statistics).

We compare this to literature values with the caveat that the galaxy samples are not matched in properties (e.g., redshift, stellar mass, depth of observation) because only a few statistical studies exist. The QPE host EELR incidence is a factor of $\sim$10 higher than the fraction of EELRs found in the galaxy sample studied by López-Cobá et al. (2020), $f_{\rm EELR}\sim0.085$. Note that a large number of these are SF- or AGN-driven outflows, which is not the case for the EELRs discovered in this work. The incidence of EELRs in QPE hosts is a factor of $\sim$30 higher than in AGN host galaxies ($f_{\rm EELR}=0.023\pm0.013$; Keel et al. 2024).

In a broader context, Keel et al. (2024) studied the EELR incidence in a large sample of AGN-hosting galaxy systems with narrowband imaging. Their results indicate that the overall EELR fractions are very low (<5%) for their sample, except for merger and post-merger galaxies, where an EELR fraction of 40%–60% is observed, similar to our result for the QPE hosts. The lack of tidal features and dust lanes in the continuum emission of most QPE hosts may indicate that the QPE hosts are not post-merger (Section 3.1), or that the merger occurred $\sim$1 Gyr ago, short enough that we still see the post-merger signatures such as extended reservoirs of gas but long enough that most obvious merger features (e.g., dust lanes, tidal tails) have already faded (Pawlik et al. 2016).

With the caveat of small sample statistics, we note that the overrepresentation of EELRs in QPE hosts is somewhat higher than that found in TDE host galaxies ($f_{\rm EELR}=0.19^{+0.14}_{-0.11}$ for the entire sample with MUSE observations; Wevers & French 2024) but consistent with the PSB/TDE/EELR host galaxies ($f_{\rm EELR}=0.6^{+0.4}_{-0.33}$; Wevers & French 2024).[16] The implication is that there may be a connection between these two classes of nuclear transients, which we explore further below.

4.1. The QPE–TDE Host Galaxy Connection

In a companion paper (Wevers & French 2024) we analyzed MUSE observations of 16 TDE host galaxies. Combined with previously known EELRs in TDE hosts, we inferred an elevated EELR incidence compared to PSB galaxies, as well as the general galaxy population.

In addition, the QPE host galaxy EELRs show peculiar kinematics that are strikingly similar to those of the EELR-hosting TDE host galaxies. The combination of nonstellar photoionization, a recently faded AGN, low velocities, and low velocity dispersions is rare among the general galaxy population (<1%), although this is based on HST narrowband imaging rather than integral field unit (IFU) observations (Keel et al. 2012, 2024). These properties are inconsistent with AGN- or shock-driven kinematics and associated ionization mechanism.

A tentative connection between the QPE phenomenon and TDEs has been proposed based on the observational properties of QPEs, including long-term declines in the continuum X-ray light curves (Miniutti et al. 2019, 2023; Arcodia et al. 2024), the presence of a single QPE-like flare in the decay of some TDE candidates (Chakraborty et al. 2021; Quintin et al. 2023), and a preference for host galaxies with QBS or PSB spectra (Wevers et al. 2022). Moreover, several theoretical models invoke partial TDEs as a mechanism to render a (preexisting) closely bound stellar remnant visible as it interacts with the newly formed, compact accretion disk. Such models strongly disfavor the presence of a large AGN accretion disk because ablation of the star would severely shorten the lifetime of the QPE source (Linial & Metzger 2024).

The tentative connection between TDEs and QPEs can also be investigated using sample properties as is done here. Our results provide the strongest, albeit indirect, indication to date that both QPE and TDE rates are enhanced in gas-rich environments with faded AGNs. There is also a possible enhancement in post-merger systems, although this statement relies on RX J1301, a PSB galaxy with merger signatures (in particular, dust lanes); QBS systems such as eRO-QPE1 are not necessarily post-merger, and while the origin of the EELRs in GSN 069 and eRO-QPE2 could in principle be related to a minor merger, this remains an open question. Most PSB galaxies show signs of a recent merger (e.g., Zabludoff et al. 1996; Pawlik et al. 2016; Sazonova et al. 2021), but such features can fade more quickly than the PSB signature (Pawlik et al. 2016).

[16] We emphasize that the sensitivity of the IFU observations is not uniform across the QPE and TDE samples.

One implication of this host galaxy connection could be that QPEs and TDEs share a common formation path. However, this depends on the theoretical scenario invoked to explain QPEs.

4.2. The QPE–EELR Connection

Our analysis shows that the QPE quiescent luminosity can in principle reach the threshold required to power the EELR energy budget (i.e., $L_{\rm QPE,quiesc} \gtrsim L_{\rm ion,min}$) in every source[17] (see Table 1). In addition, the quiescent QPE luminosities of the two host galaxies without EELRs are the lowest among the sample. The implication is that it may, in principle, be possible that the QPE quiescent luminosity is the powering source of the EELRs. This would, in turn, require the presence of a long-lived accretion flow. In contrast, with the low duty cycle of QPEs (∼25%, Guolo et al. 2024) and their unknown but likely limited lifetime,[18] it appears improbable that the eruptions alone can power the EELRs.

Some QPE scenarios require a (partial) TDE to occur before QPEs can be detected. As TDEs typically have a larger energy budget available, it is in principle possible to power the EELRs through a (time-limited) increase in the TDE rate by a factor of ∼10 compared to the average TDE rate in PSB galaxies (Wevers & French 2024). Depending on the relative rates of TDEs and QPEs, it may therefore also be possible that the EELRs are powered (in part) by episodic accretion in the form of an elevated TDE rate and the associated (compact) accretion disks, rather than a classical AGN phase.

4.3. Implications for the Nature of QPEs

4.3.1. Partial TDE Scenario

The fact that both QPEs and TDEs prefer host galaxies with similar, peculiar properties can point to an intrinsic connection between these classes of events. In this case, the most obvious link may be through the disturbed state of the galactic nuclei following a (minor) galaxy merger. This would perturb the orbits of stars in the nucleus and lead to an increased rate of star–SMBH encounters of all kinds, including full tidal disruptions, partial TDEs, and even direct captures. QPEs have been linked to partial TDEs, where the Hills mechanism can disrupt a binary star system to capture one of the components on a tight eccentric orbit, leading to the repeated partial stripping at each pericenter passage or alternatively direct mass transfer (e.g., King 2022; Krolik & Linial 2022; Metzger et al. 2022; Zhao et al. 2022; Linial & Sari 2023; Lu & Quataert 2023). In the eccentric case, gas overflows the Roche lobe of a star near pericenter passage, forming an accretion disk to produce the observed X-ray emission and the periodic injections of more gas. For the circular case, Roche lobe overflow in the presence of a companion star leads to the observed quasi-periodicity. In this scenario, repeating nuclear transients on all timescales would likely share a common formation channel and therefore host galaxy preference, even though they may not share the same observational properties (e.g., Guolo et al. 2024). This idea can be tested through a host galaxy study of a more inclusive set of repeating nuclear transients, including QPEs and partial TDEs recurring on timescales of tens to thousands of days (e.g., Payne et al. 2021; Liu et al. 2023; Wevers et al. 2023; Guolo et al. 2024).

4.3.2. Star−Disk/BH−Disk Interaction Scenario

In addition to the partial TDE scenario, there exist related but distinct theoretical models to explain QPEs. For example, the rate and lifetime of extreme mass ratio inspiral systems (EMRIs) is sufficiently high that a preexisting bound stellar-mass companion is expected to be present in numerous galactic nuclei (Linial & Metzger 2024). Rendering such systems visible is possible if a TDE provides a compact accretion disk with which the bound remnant periodically interacts, leading to the QPE phenomenon (Linial & Metzger 2023). In this scenario there is a natural commonality between the host galaxies of QPEs and TDEs, as the latter are required to observe the former. One distinction with the pTDE models is that the typical lifetime of the QPE (set by the ablation timescale of the star while interacting with the disk) is at most 1000 yr. A preference for PSB galaxies was predicted in this scenario, as such systems are more likely to host EMRIs in the first place (Metzger et al. 2022). Given that the EELR sizes are >10,000 lt-yr, powering the EELRs with QPEs would require a succession of EMRI captures, as well as TDEs on timescales shorter than the typical QPE lifetime (i.e., rates in excess of 10^{-3} galaxy^{-1} yr^{-1}). While EMRI rates are highly uncertain, this high rate appears incompatible with the average TDE rate of a few $\times$ 10^{-5} galaxy^{-1} yr^{-1} (e.g., Sazonov et al. 2021; Yao et al. 2023) but may be within range for PSB galaxies specifically (French et al. 2020).

4.3.3. Accretion Disk Instability Scenario

Alternatively, QPEs have also been suggested to be caused by instabilities in large AGN-like disks (e.g., Sniegowska et al. 2020; Raj & Nixon 2021; Pan et al. 2023). On one hand, it seems less likely that the connection between QPEs and TDEs is intrinsic in this case. The TDEs found in EELR-hosting galaxies are unremarkable in the context of the known TDE sample, while it has been predicted that AGN disks may significantly alter the observed properties (Chan et al. 2019). On the other hand, it has been proposed that the presence of an AGN disk may significantly increase the TDE rate (e.g., Kennedy et al. 2016; Kaur & Stone 2024; Wang et al. 2024). All three QPE nuclei with EELRs have faded in the recent past, which has been suggested to result in a higher TDE rate owing to star−disk interactions and the presence of stars formed in the outer regions of the accretion disk (Wang et al. 2024), or alternatively via an enhanced loss cone filling rate through collisionless processes in gas-rich nuclei (Kaur & Stone 2024).

We highlight that, based on X-ray spectral modeling, the neutral (and ionizing) absorbing columns are very low: $N_{\rm H} \simeq 4 \times 10^{21}$ cm^{-2} ($E(B-V) \sim 0.6$; Güver & Özel 2009) for eRO-QPE2 and $N_{\rm H} < 5 \times 10^{20}$ cm^{-2} ($E(B-V) < 0.07$) for all others, i.e., QPE nuclei are completely unobscured. Nevertheless, no BELs are detectable in deep long-slit data (Wevers et al. 2022) or in our MUSE observations. For the source GSN 069, the present-day continuum (quiescent) bolometric luminosity is of order a few $\times$ 10^{43} erg s^{-1}, and hence this lack of BELs is unlikely to be the consequence of a too-low nuclear luminosity. Instead, it may be related to the presence of a disk that is too compact to support a typical broad-line region

[17] Note that the long-term luminosity behavior may be highly variable.
[18] In the star−disk interaction models, it is <1000 yr (Linial & Metzger 2024).

(BLR), which is compatible with the accretion disks that form in the aftermath of a TDE (for which several lines of evidence exist in GSN 069; Sheng et al. 2021; Miniutti et al. 2023; Patra et al. 2024). Pan et al. (2023) argue that while QPEs do require some fine-tuning (a very small unstable region, peculiar magnetic field, etc.), it is possible, in principle, that these conditions are only met in compact TDE disks but inefficient in much larger AGN disks.

The current weak state of the nuclei (compared to a more luminous state in the past, required by the EELR energy budget) may be the result of a selection bias against QPEs in higher-luminosity AGNs. It may be more difficult to detect the QPEs as an additional component on top of the AGN continuum emission (Miniutti et al. 2023), which may be highly variable, especially so for low black hole masses (e.g., Ponti et al. 2012). Similarly, the TDE detection rate may be biased against AGN host galaxies because of spectroscopic selection biases. In this scenario the selection biases in both TDEs and QPEs would need to conspire to create the observed similarities and the preferences for an extremely rare type of host galaxy. This scenario is somewhat contrived, but ruling it out completely will only be possible with larger samples of QPE and TDE host galaxies.

4.4. Localization of Low-frequency Gravitational-wave Sources

Maximizing the scientific value of gravitational-wave (GW) sources will be facilitated by complementary electro-magnetic (EM) information such as the host redshift, galaxy/black hole mass, and stellar population properties. Due to the poor sky localization of LISA GW detections (typically of order a degree or larger), the number of galaxies within the error volume will be very large (Lops et al. 2023). Simulations show that it is very challenging to uniquely identify the host galaxies of GW sources. This is because the preferred host galaxies are dwarfs with merger signatures, but a large fraction of the dwarf galaxy population will exhibit very similar signatures (Izquierdo-Villalba et al. 2023).

However, we have found that QPE sources (as well as TDEs; Wevers & French 2024) are strongly overrepresented in galaxies hosting recently faded AGNs and large EELRs with peculiar kinematical properties. Galaxies with similar properties are very rare among the general galaxy population; hence, if the association of QPEs with stellar-mass EMRIs can be confirmed, these peculiar properties can be used to improve the fidelity of EMRI host galaxy localization, which will help to maximize the scientific return of GW astronomy.

Because the X-ray eruptions have a low duty cycle (Guolo et al. 2024) and potentially short lifetimes (<1000 yr; e.g., Linial & Metzger 2023), it is likely that QPEs will be detected in only a small subset of GW detections (e.g., Franchini et al. 2023, who show that only $\sim$2% of BH EMRIs would produce detectable QPEs). Making associations through their host galaxies can therefore be a valuable complementary method to find EM counterparts.

5. Conclusions

We report on the analysis of MUSE integral field spectroscopy of the host galaxies of five X-ray QPE sources. The sensitivity, large field of view, and small spaxel size of MUSE provide an unprecedented, spatially resolved view of the QPE host galaxies. We measure the stellar and emission-line kinematics, fluxes, and flux ratios to characterize their properties.

We find that three out of five galaxies have EELRs that have low velocities that are decoupled from the stellar motions. The emission-line ratios require a hard nonstellar continuum as the source of the ionizing photons, but the very narrow line velocity dispersions and low velocities are inconsistent with these EELRs being driven by a currently active nucleus. Furthermore, no BELs are observed, which, together with the lack of significant obscuration, could suggest that no classical BLR is present.[19]

The present-day nuclear luminosity estimated from FIR observations is insufficient to satisfy the EELR energy budgets, implying that the putative AGNs in these nuclei have decreased their luminosity output significantly compared to the most stringent constraints on the luminosity history available using the EELRs (which trace the accretion history over 9000–30,000 lt-yr, a size limited by the density of the circumgalactic gas). This could suggest a connection between either the intrinsic rate or the detection rate of QPEs and the specific phase in the AGN duty cycle. The overrepresentation of EELRs in the QPE host galaxies is comparable to AGN-hosting merger/post-merger systems and significantly elevated compared to the general galaxy population.

Several properties of the QPE host galaxies are similar to those of TDE host galaxies. Both classes have a preference for QBS/PSB galaxies (French et al. 2016; Wevers et al. 2022), a strong overrepresentation of EELRs with recently faded nuclei, and peculiar ionized gas kinematic properties (studied in detail for TDE hosts in Wevers & French 2024). The rarity of the preferred type of host galaxies is highly unlikely to be due to chance and is robust against associations based on the unique properties of individual QPE sources. This strongly suggests a connection between these two classes of events, consistent with theoretical arguments and hinted at in the observational properties of individual sources (Miniutti et al. 2023; Arcodia et al. 2024).

The proposed link between QPEs and TDEs disfavors AGN accretion disk models as the origin of QPEs, as (i) the AGNs are currently inactive and (ii) this would be the result of two independent selection biases (a detection bias for QPEs, and a detection and/or classification bias for TDEs). The instabilities proposed as the origin for QPEs are typically not "standard" thermal instabilities. Most require some fine-tuning (e.g., magnetic fields inducing very small unstable regions, or independently precessing rings in the case of disk tearing) that are not expected in long-lived large AGN-like disks.

More detailed studies, including deep narrowband imaging and/or higher spatial resolution IFU observations, of both QPE and TDE host galaxies can be used to further test the similarity of the host galaxy preferences of these transients. Larger samples can be used to further characterize the properties of these host galaxies and predictions for EMRI GW sources. If these galaxies can be typed by machine learning algorithms, this may facilitate the localization of low-frequency GW detections with future observatories.

[19] We note that our observations do not have sufficient spatial resolution to robustly rule out the presence of faint BELs.

Acknowledgments

We are grateful to D. Kakkad, W. Lu, and S. van Velzen for discussions and suggestions; to M. Giustini for providing a recent quiescent luminosity estimate of RX J1301; and to J. Depasquale for creating the composite color images in Figure 1. We thank the reviewer for a thoughtful and constructive report that improved the clarity of the manuscript. K.D.F. acknowledges support from NSF grant AAG 22-06164. G.M. was supported by grant PID2020-115325GB-C31 funded by MICIN/AEI/10.13039/501100011033. A.I.Z. acknowledges support from NASA ADAP grant 80NSSC21K0988. I.L. acknowledges support from a Rothschild Fellowship and the Gruber Foundation. Based on observations collected at the European Southern Observatory under ESO programs 109.238W.007, 111.24UJ.005, and 113.26F6.001. This research was supported in part by grant NSF PHY-2309135 to the Kavli Institute for Theoretical Physics (KITP). We thank the organizers of the KITP program "Toward a Physical Understanding of Tidal Disruption Events," where part of this work was performed.

Facility: ESO/VLT.
Software: astropy (Astropy Collaboration et al. 2013, 2018).

Appendix A
Supplementary Material

A.1. Data Reduction

The MUSE data are reduced and combined following the instrument pipeline as described in Weilbacher et al. (2020). An absolute flux calibration is derived using spectrophotometric standard stars and has a typical uncertainty of 4%–7%. The astrometric precision is typically a quarter of a spatial element or better, while the dispersion in the wavelength solution as measured from a single arc line is 2–4 km s^{-1}, although the latter can be improved by measuring multiple lines simultaneously.

Figure A1 shows the continuum datacubes of eRO-QPE1 and eRO-QPE3, the two sources without a detected EELR, overlaid with Hα line flux contours. Table A2 provides an overview of the QPE host galaxy properties studied in this work, and Table A1 gives a full observing log.

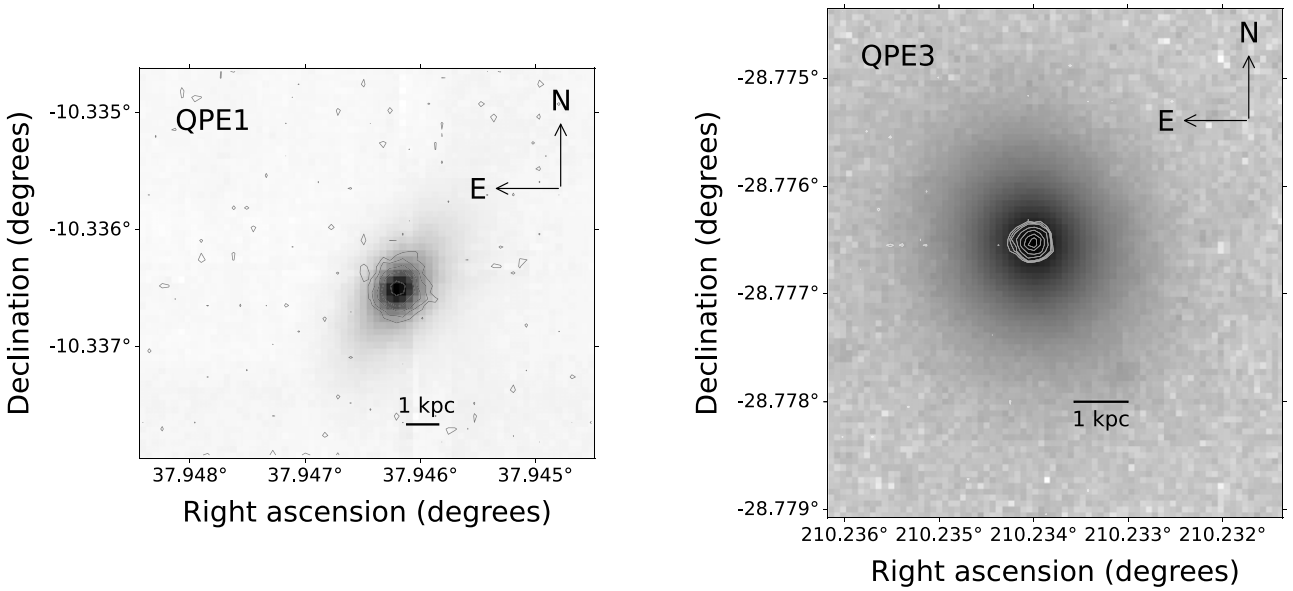

Figure A1. Continuum grayscale image and Hα contours overlaid for sources eRO-QPE1 (left) and eRO-QPE3 (right), which do not show an EELR. The faintest contours represent Hα flux levels of 35×10^{-20} erg cm^{-2} s^{-1} Å and 15×10^{-20} erg cm^{-2} s^{-1} Å for eRO-QPE1 and eRO-QPE3, respectively.

Table A1
Overview of the QPE Host Galaxies Analyzed in This Work

Source	z	Spatial resolution (pc pixel^{-1})	PSF FWHM (arcsec)	PSF FWHM (pc)	$E(B-V)_{\rm gal}$ (mag)	$\sigma_{\rm star}$ (km s^{-1})	Reference
GSN 069	0.0182	74	1.0	370	0.0232	68 ± 12	Saxton et al. (2011)
RX J1301	0.0237	96	0.94*	450	0.0077	68 ± 5	Dewangan et al. (2000)
eRO-QPE1	0.0505	199	0.95*	940	0.0212	66 ± 4	Arcodia et al. (2021)
eRO-QPE2	0.0175	71	0.7	250	0.0153	38 ± 6	Arcodia et al. (2021)
eRO-QPE3	0.024	97	0.7	340	0.0505	38 ± 5	Arcodia et al. (2024)

Note. Spatial resolution refers to the native 0.″2 pixel scale of the MUSE WFM-NOAO observations. The PSF FWHM is estimated using point sources in the continuum cube when available, or otherwise taken as the average seeing conditions (uncorrected for air mass) provided by the observatory (marked with an asterisk) as tabulated in Table A2. Parameter $\sigma_{\rm star}$ provides the central velocity dispersion, measured using an aperture with the size of the PSF FWHM.

Table A2
Observing Log of the VLT/MUSE Data

Source	Date (MJD)	Exposure Time (s)	Air Mass	DIMM Seeing (arcsec)
GSN 069	59787.237738	1497	1.64	0.53
	59787.256443	1497	1.46	0.73
RX J1301	59787.966968	1497	1.92	1.10
	59787.985819	1497	2.11	0.78
eRO-QPE1	59834.144255	1497	2.25	1.11
	59834.162944	1497	1.86	0.75
	59834.263008	1497	1.11	1.03
	59834.281717	1497	1.07	1.04
	59834.303142	1497	1.04	0.74
	59834.321856	1497	1.03	0.87
	59834.343499	1497	1.04	1.04
	59834.362185	1497	1.06	0.98
eRO-QPE2	59787.369579	1497	1.18	0.63
	59787.388267	1497	1.13	0.51
	59814.263422	1497	1.30	2.19
	59814.282118	1497	1.23	0.97
eRO-QPE3	60416.343266	1497	1.352	4.84
	60416.361829	1498	1.498	4.84
	60432.108992	1492	1.060	0.33
	60432.127534	1493	1.029	0.44
	60435.208337	1480	1.041	1.21
	60435.226639	1480	1.078	1.16
	60438.139092	1487	1.005	0.81
	60438.157507	1488	1.003	0.64
	60439.167192	1486	1.008	0.78
	60439.185699	1486	1.025	0.85

Note. All data were taken in Wide Field no-AO Mode with the nominal filter.

Appendix B
Full Spectrum Fitting with PPXF

To constrain the kinematics of the gas and the stars, we employ the full spectrum fitting code PPXF (Cappellari 2017, 2023). We use the MILES SSP template library (Vazdekis et al. 2015) to model the stellar continuum contribution to the spectra. We use models with a Kroupa initial mass function and sample a range of metallicities ($Z =$ −1.71 to 0.22) and stellar ages (0.063–15.85 Gyr). We mask out 2000 km s^{-1} around the H Balmer lines and 1000 km s^{-1} around prominent emission lines, the Na I D doublet, and telluric lines. To fit the stellar continuum, we fit the first two moments of the kinematics (V and σ) and do not use multiplicative or additive polynomials. We then add the ionized gas component to the best-fit stellar continuum for every spaxel. The ionized gas kinematics are constrained through a joint fit of the emission lines, although decoupling the lines does not significantly change the results. The resulting emission-line fluxes are corrected for stellar absorption. To measure the stellar velocity dispersion, we follow the methodology outlined in Wevers et al. (2017) to obtain a measurement and uncertainty using 1000 simulated spectra.

Figure B1 shows the resulting emission line maps, highlighting the nuclear regions of the galaxies. Figures B2, B3, and B4 show the spectra for the apertures defined in the second row of Figure 1. The velocity dispersion maps are shown in Figure B5, while the Figure B6 shows the BPT diagram of the resulting line ratios for eRO-QPE3. The constraints on the ionizing luminosity are derived from Figure B7, and the results of the Bagpipes SFH modeling are shown in Figure B8.

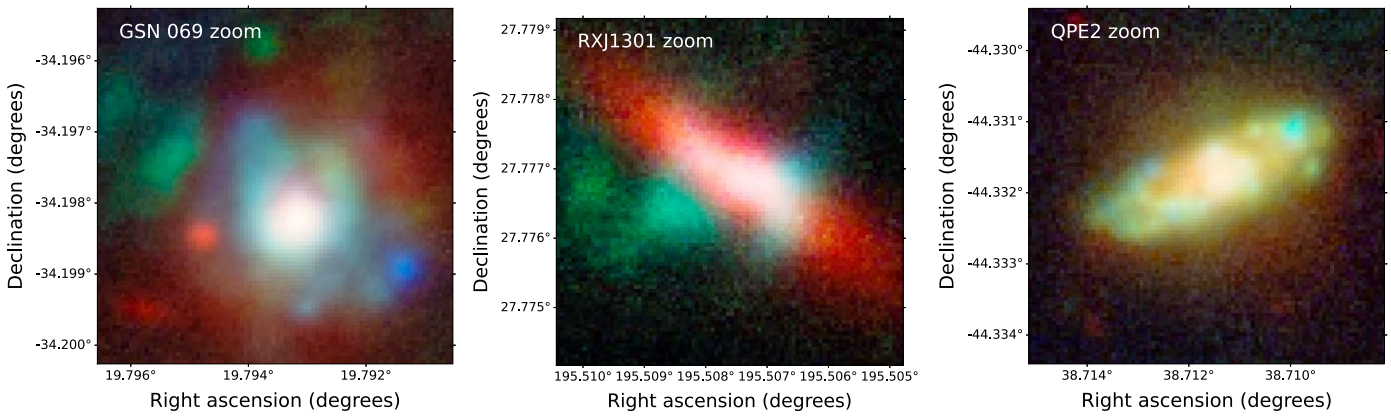

Figure B1. Same as the top row of Figure 1, but zoomed in to improve the detailed view of the nuclear regions of the galaxies. Note the presence of a ringlike structure surrounding the nucleus of GSN 069, which may be a star-forming ring.

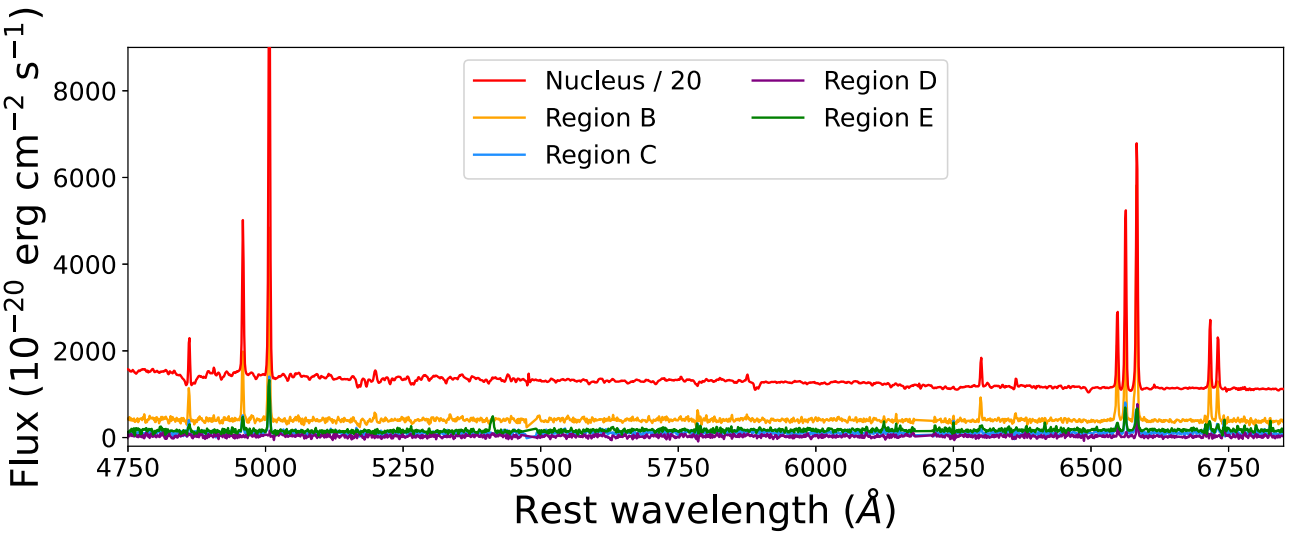

Figure B2. Aperture spectra of GSN 069, for the regions indicated in Figure 1, with the same color-coding.

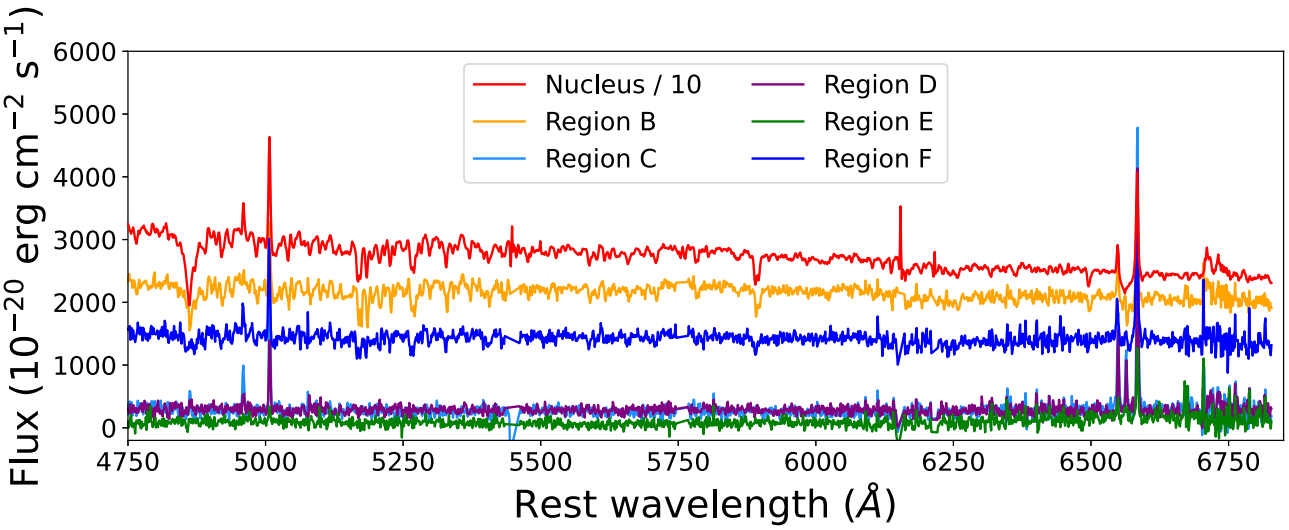

Figure B3. Aperture spectra of RX J1301, for the regions indicated in Figure 1, with the same color-coding.

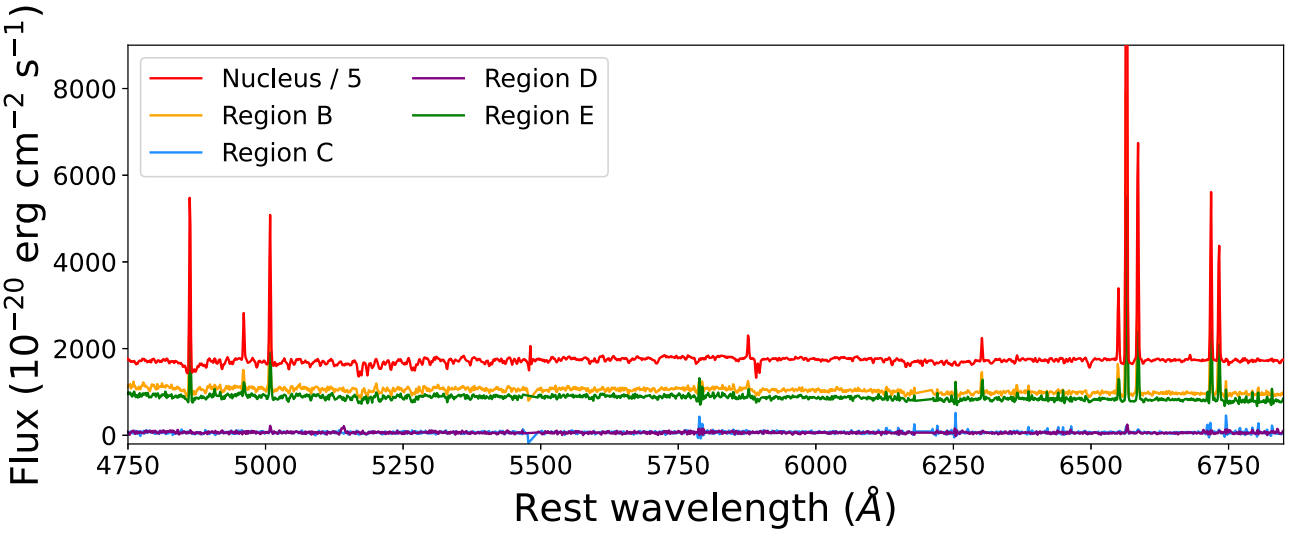

Figure B4. Aperture spectra of eRO-QPE2, for the regions indicated in Figure 1, with the same color-coding.

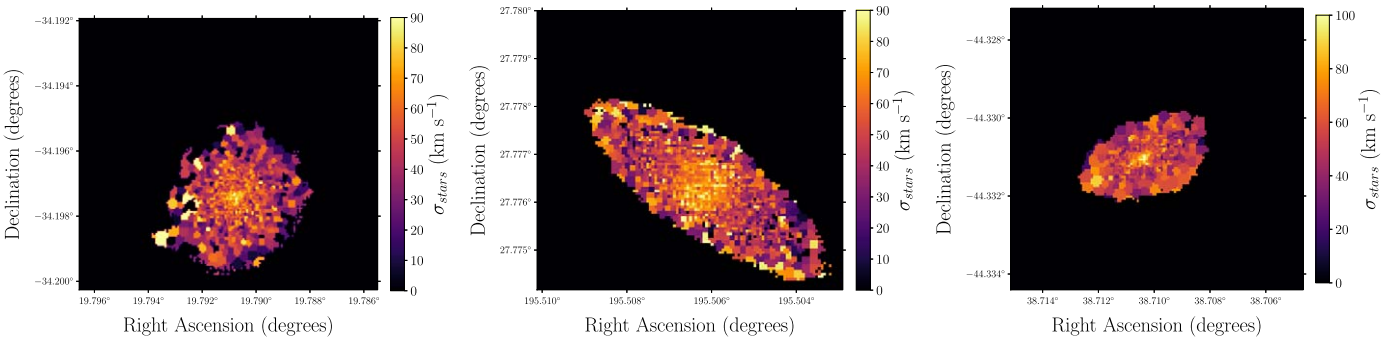

Figure B5. Stellar velocity dispersion maps of GSN 069 (left), RX J1301 (middle), and eRO-QPE2 (right).

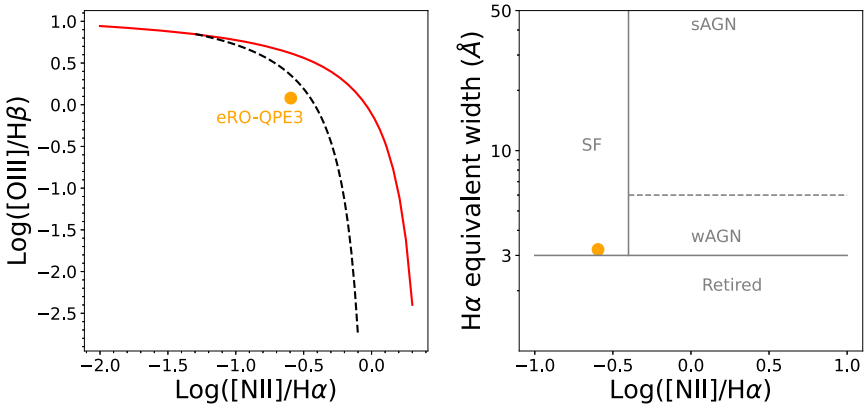

Figure B6. BPT and WHAN diagrams for the source eRO-QPE3.

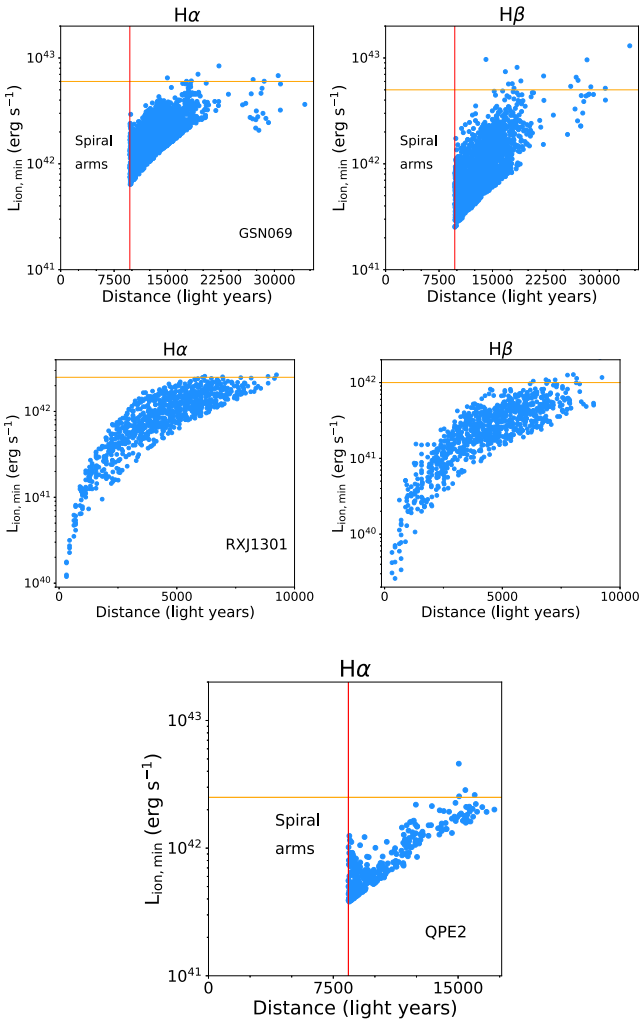

Figure B7. Constraints on the ionizing luminosity. Every data point represents the minimum required ionizing luminosity to explain the EELR (indicated by the orange horizontal line), assuming recombination balance, for an individual spaxel. The inner regions of GSN 069 and eRO-QPE2 are actively star-forming, so they are excluded for clarity (marked by the red vertical lines).

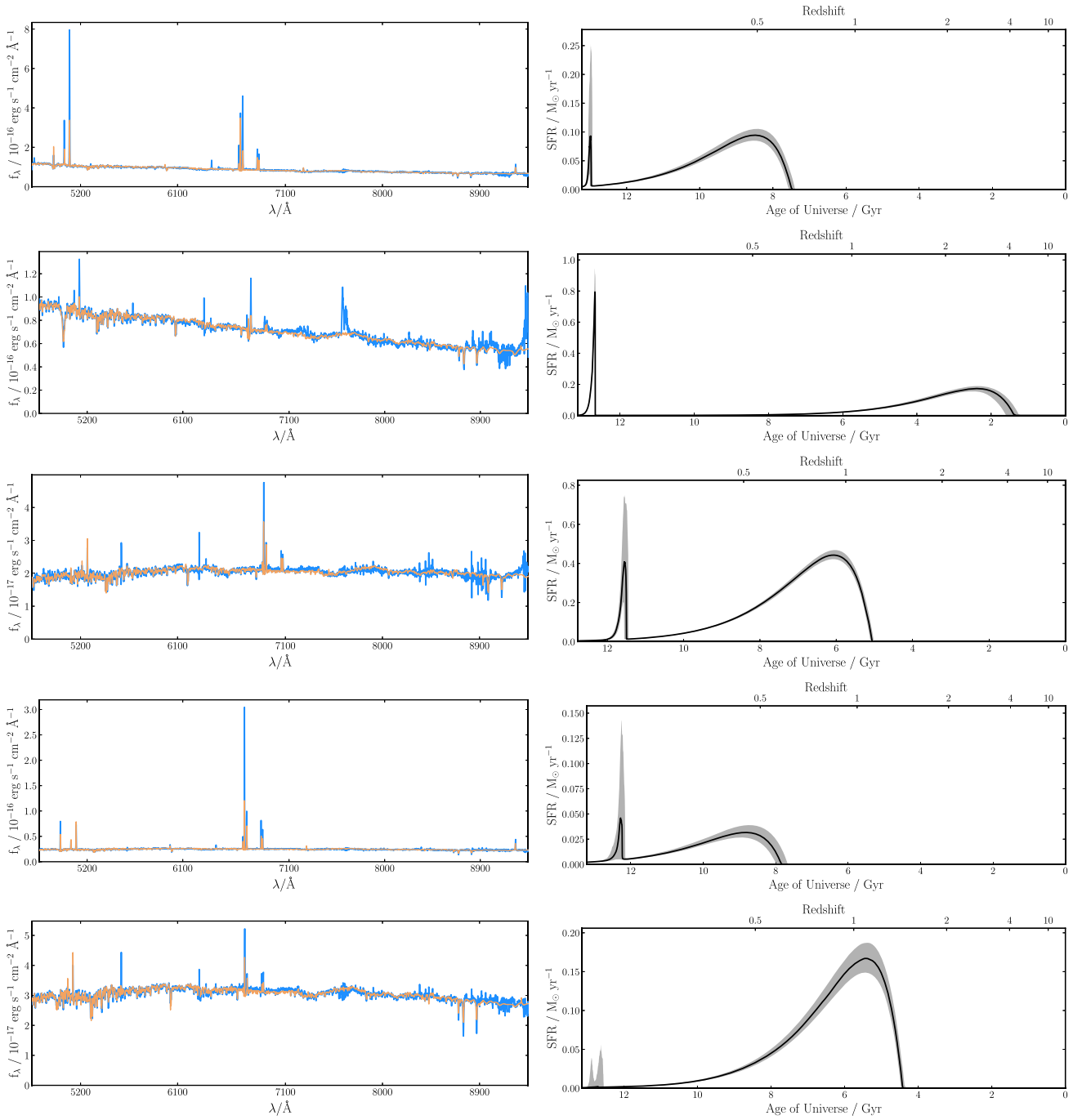

Figure B8. Bagpipe fits and inferred SFH, assuming a double starburst as detailed in the text. From top to bottom: GSN 069, RX J1301, eRO-QPE1, eRO-QPE2, and eRO-QPE3.

ORCID iDs

T. Wevers https://orcid.org/0000-0002-4043-9400
K. D. French https://orcid.org/0000-0002-4235-7337
A. I. Zabludoff https://orcid.org/0000-0001-6047-8469
T. C. Fischer https://orcid.org/0000-0002-3365-8875
K. Rowlands https://orcid.org/0000-0001-7883-8434
M. Guolo https://orcid.org/0000-0002-5063-0751
B. Dalla Barba https://orcid.org/0009-0007-1729-2352
R. Arcodia https://orcid.org/0000-0003-4054-7978
M. Berton https://orcid.org/0000-0002-1058-9109
F. Bian https://orcid.org/0000-0002-1620-0897
I. Linial https://orcid.org/0000-0002-8304-1988
G. Miniutti https://orcid.org/0000-0003-0707-4531
D. R. Pasham https://orcid.org/0000-0003-1386-7861

References

Arcodia, R., Liu, Z., Merloni, A., et al. 2024, A&A, 684, A64
Arcodia, R., Merloni, A., Nandra, K., et al. 2021, Natur, 592, 704
Astropy Collaboration, Price-Whelan, A. M., Sipőcz, B. M., et al. 2018, AJ, 156, 123
Astropy Collaboration, Robitaille, T. P., Tollerud, E. J., et al. 2013, A&A, 558, A33
Bacon, R., Accardo, M., Adjali, L., et al. 2010, Proc. SPIE, 7735, 773508
Baron, D., Netzer, H., Lutz, D., Prochaska, J. X., & Davies, R. I. 2022, MNRAS, 509, 4457

Calzetti, D., Armus, L., Bohlin, R. C., et al. 2000, ApJ, 533, 682
Cappellari, M. 2017, MNRAS, 466, 798
Cappellari, M. 2023, MNRAS, 526, 3273
Carnall, A. C., McLure, R. J., Dunlop, J. S., & Davé, R. 2018, MNRAS, 480, 4379
Carnall, A. C., McLure, R. J., Dunlop, J. S., et al. 2019, MNRAS, 490, 417
Chakraborty, J., Arcodia, R., Kara, E., et al. 2024, ApJ, 965, 12
Chakraborty, J., Kara, E., Masterson, M., et al. 2021, ApJL, 921, L40
Chan, C.-H., Piran, T., Krolik, J. H., & Saban, D. 2019, ApJ, 881, 113
Dewangan, G. C., Singh, K. P., Mayya, Y. D., & Anupama, G. C. 2000, MNRAS, 318, 309
Fischer, T. C., Crenshaw, D. M., Kraemer, S. B., & Schmitt, H. R. 2013, ApJS, 209, 1
Franchini, A., Bonetti, M., Lupi, A., et al. 2023, A&A, 675, A100
French, K. D., Arcavi, I., & Zabludoff, A. 2016, ApJL, 818, L21
French, K. D., Earl, N., Novack, A. B., et al. 2023, ApJ, 950, 153
French, K. D., Wevers, T., Law-Smith, J., Graur, O., & Zabludoff, A. I. 2020, SSRv, 216, 32
Gehrels, N. 1986, ApJ, 303, 336
Giustini, M., Miniutti, G., & Saxton, R. D. 2020, A&A, 636, L2
Graur, O., French, K. D., Zahid, H. J., et al. 2018, ApJ, 853, 39
Gültekin, K., Richstone, D. O., Gebhardt, K., et al. 2009, ApJ, 698, 198
Guolo, M., Pasham, D. R., Zajaček, M., et al. 2024, NatAs, 8, 347
Güver, T., & Özel, F. 2009, MNRAS, 400, 2050
Hafen, Z., Faucher-Giguère, C.-A., Anglés-Alcázar, D., et al. 2019, MNRAS, 488, 1248
Izquierdo-Villalba, D., Colpi, M., Volonteri, M., et al. 2023, A&A, 677, A123
Johnston, K. V., Bullock, J. S., Sharma, S., et al. 2008, ApJ, 689, 936
Kaur, K., & Stone, N. C. 2024, arXiv:2405.18500
Keel, W. C., Chojnowski, S. D., Bennert, V. N., et al. 2012, MNRAS, 420, 878
Keel, W. C., Lintott, C. J., Maksym, W. P., et al. 2017, ApJ, 835, 256
Keel, W. C., Maksym, W. P., Bennert, V. N., et al. 2015, AJ, 149, 155
Keel, W. C., Moiseev, A., Uklein, R., & Smirnova, A. 2024, MNRAS, 530, 1624
Kennedy, G. F., Meiron, Y., Shukirgaliyev, B., et al. 2016, MNRAS, 460, 240
King, A. 2022, MNRAS, 515, 4344
Krolik, J. H., & Linial, I. 2022, ApJ, 941, 24
Kroupa, P. 2001, MNRAS, 322, 231
Linial, I., & Metzger, B. D. 2023, ApJ, 957, 34
Linial, I., & Metzger, B. D. 2024, arXiv:2404.12421
Linial, I., & Sari, R. 2023, ApJ, 945, 86
Liu, Z., Malyali, A., Krumpe, M., et al. 2023, A&A, 669, A75
López-Cobá, C., Sánchez, S. F., Anderson, J. P., et al. 2020, AJ, 159, 167
Lops, G., Izquierdo-Villalba, D., Colpi, M., et al. 2023, MNRAS, 519, 5962
Lu, W., & Quataert, E. 2023, MNRAS, 524, 6247
Metzger, B. D., Stone, N. C., & Gilbaum, S. 2022, ApJ, 926, 101
Miniutti, G., Giustini, M., Arcodia, R., et al. 2023, A&A, 670, A93
Miniutti, G., Saxton, R. D., Giustini, M., et al. 2019, Natur, 573, 381
Mockler, B., Guillochon, J., & Ramirez-Ruiz, E. 2019, ApJ, 872, 151
Pan, X., Li, S.-L., & Cao, X. 2023, ApJ, 952, 32
Patra, K. C., Lu, W., Ma, Y., et al. 2024, MNRAS, 530, 5120
Pawlik, M. M., Wild, V., Walcher, C. J., et al. 2016, MNRAS, 456, 3032
Payne, A. V., Shappee, B. J., Hinkle, J. T., et al. 2021, ApJ, 910, 125
Ponti, G., Papadakis, I., Bianchi, S., et al. 2012, A&A, 542, A83
Quintin, E., Webb, N. A., Guillot, S., et al. 2023, A&A, 675, A152
Raj, A., & Nixon, C. J. 2021, ApJ, 909, 82
Saxton, R., Read, A., Esquej, P., Miniutti, G., & Alvarez, E. 2011, arXiv:1106.3507
Sazonov, S., Gilfanov, M., Medvedev, P., et al. 2021, MNRAS, 508, 3820
Sazonova, E., Alatalo, K., Rowlands, K., et al. 2021, ApJ, 919, 134
Schawinski, K., Koss, M., Berney, S., & Sartori, L. F. 2015, MNRAS, 451, 2517
Schlafly, E. F., & Finkbeiner, D. P. 2011, ApJ, 737, 103
Schweizer, F., Seitzer, P., Kelson, D. D., Villanueva, E. V., & Walth, G. L. 2013, ApJ, 773, 148
Sheng, Z., Wang, T., Ferland, G., et al. 2021, ApJL, 920, L25
Sniegowska, M., Czerny, B., Bon, E., & Bon, N. 2020, A&A, 641, A167
Tagawa, H., & Haiman, Z. 2023, MNRAS, 526, 69
Vazdekis, A., Coelho, P., Cassisi, S., et al. 2015, MNRAS, 449, 1177
Wang, M., Ma, Y., Wu, Q., & Jiang, N. 2024, ApJ, 960, 69
Weaver, J., Husemann, B., Kuntschner, H., et al. 2018, A&A, 614, A32
Weilbacher, P. M., Palsa, R., Streicher, O., et al. 2020, A&A, 641, A28
Wevers, T., Coughlin, E. R., Pasham, D. R., et al. 2023, ApJL, 942, L33
Wevers, T., & French, K. D. 2024, ApJL, 969, L17
Wevers, T., Pasham, D. R., Jalan, P., Rakshit, S., & Arcodia, R. 2022, A&A, 659, L2
Wevers, T., Stone, N. C., van Velzen, S., et al. 2019, MNRAS, 487, 4136
Wevers, T., van Velzen, S., Jonker, P. G., et al. 2017, MNRAS, 471, 1694
Wild, V., Heckman, T., & Charlot, S. 2010, MNRAS, 405, 933
Yao, Y., Ravi, V., Gezari, S., et al. 2023, ApJL, 955, L6
Zabludoff, A. I., Zaritsky, D., Lin, H., et al. 1996, ApJ, 466, 104
Zhao, Z. Y., Wang, Y. Y., Zou, Y. C., Wang, F. Y., & Dai, Z. G. 2022, A&A, 661, A55
Zhou, C., Zhong, B., Zeng, Y., Huang, L., & Pan, Z. 2024, arXiv:2405.06429